Electrical analysis of inter-growth structured $Bi_4Ti_3O_{12}$–$Na_{0.5}Bi_{4.5}Ti_4O_{15}$ ceramics*

Xiangping Jiang(江向平), Yalin Jiang(江亚林), Xingan Jiang(江兴安)†, Chao Chen(陈超)‡, Na Tu(涂娜), and Yunjing Chen(陈云婧)

Jiangxi Key Laboratory of Advanced Ceramic Materials, Department of Material Science and Engineering, Jingdezhen Ceramic Institute, Jingdezhen 333001, *China*

(Received 15 December 2016; revised manuscript received 2 April 2017; published online 17 May 2017)

Inter-growth bismuth layer-structured ferroelectrics (BLSFs), $Bi_4Ti_3O_{12}-Na_{0.5}Bi_{4.5}Ti_4O_{15}$ (BIT–NBT), were successfully synthesized using the traditional solid-state reaction method. X-ray diffraction (XRD) Rietveld refinements were conducted using GSAS software. Good agreement and low residual are obtained. The XRD diffraction peaks can be well indexed into *I*2*cm* space group. The inter-growth structure was further observed in the high-resolution TEM image. Dielectric and impedance properties were measured and systematically analyzed. At the temperature range 763–923 K (below T_c), doubly ionized oxygen vacancies (OVs) are localized and the short-range hopping leads to the relaxation processes with an activation energy of 0.79–1.01 eV. Above T_c, the doubly charged OVs are delocalized and become free ones, which contribute to the long-range dc conduction. The reduction in relaxation species gives rise to a higher relaxation activation energy $\sim$ 1.6 eV.

Keywords: $Bi_4Ti_3O_{12}-Na_{0.5}Bi_{4.5}Ti_4O_{15}$, impedance spectroscopy, oxygen vacancies-related defect dipoles, electrical analysis

PACS: 77.65.Bn, 77.80.B–, 77.84.–s **DOI:** 10.1088/1674-1056/26/7/077701

1. Introduction

In 1976, Kikuchi first reported inter-growth bismuth layer-structured ferroelectrics (IBLSFs) $Bi_7Ti_4NbO_{21}$ and $Bi_6Ti_3WO_{18}$, and they suggested that the new compounds could be characterized by a combination of two known BLSFs formulas, i.e., $Bi_4Ti_3O_{12}$ ($m = 3$) and Bi_3TiNbO_9 ($m = 2$) for $Bi_7Ti_4NbO_{21}$, and $Bi_4Ti_3O_{12}$ and Bi_2WO_6 ($m = 1$) for $Bi_6Ti_3WO_{18}$.[1] Later on, a series of mixed-layer-type compounds were widely reported in literature, such as $Bi_5TiNbWO_{15}$, $Na_{0.5}Bi_{4.5}Nb_2WO_{15}$, $Bi_7Ti_4TaO_{21}$, $M^IBi_6Ti_3Nb_2O_{21}$ (M^I = Sr, Ba), and $M^{II}Bi_8Ti_7O_{27}$ (M^{II} = Ca, Sr, Ba, Pb and $Na_{0.5}Bi_{0.5}$).[2–7] To date, most investigations of IBLSFs have been performed to elucidate their fundamental properties. Enhanced ferro/piezo-electric properties have been generally discovered in these IBLSFs materials, which are rationally attributed to the quite distinct type of Bi^{3+} ionic displacements along the *a* axis in the Bi_2O_2 layers arising from the mismatch between the two composed separate units and their respective chemical character.[3,4] For meeting the requirements of ferroelectric application, low dielectric loss is another important consideration. However, these IBLSFs materials generally suffer from prominent dielectric loss especially at high temperatures. Worse still, it was reported that dielectric measurements on some of these compounds could not even be conducted at temperatures above 400 °C due to the dramatic increase in the electric conductivity.[2] In this regard, explorations of the electrical behaviors at high temperatures are of urgent requirement and significant importance for developing the family of IBLSFs compounds. But still, there are only a few reports dealing with this work.

In the present work, we successfully synthesize inter-growth structured ceramics $Bi_4Ti_3O_{12}$–$Na_{0.5}Bi_{4.5}Ti_4O_{15}$ (BIT–NBT) through a solid-state reaction route. Our efforts are made to tentatively characterize their structure and study the dielectric and conductivity behaviors at high temperatures above 400 °C.

2. Experiment

$Bi_4Ti_3O_{12}$–$Na_{0.5}Bi_{4.5}Ti_4O_{15}$ (BIT–NBT) ceramics were synthesized via the conventional solid-state reaction method. Analytical grades Na_2CO_3 (99.8%), TiO_2 (99.0%), and Bi_2O_3 (99.0%) were weighed accurately, ball-milled in polyethylene bottles for 24 h, and calcinated at 770 °C for 3 h. Then, the calcinated mixture was ground, and pressed under 18 MPa into pellets of approximately 13 mm in diameter and about 0.8 mm in thickness. The pressed disks were finally sintered in the air-tight crucible at 1070 °C for 4 h and then cooled naturally to room temperature.

X-ray diffraction (XRD) data were obtained by an x-ray diffractometer (D8 Advanced, Bruker axs, Germany). Rietveld refinement on XRD data was performed using GSAS software. TEM images were obtained by high-resolution

*Project supported by the National Natural Science Foundation of China (Grant Nos. 51562014, 51262009, and 51602135).

†Corresponding author. E-mail: XINGAN.JIANG@Yahoo.com

‡Corresponding author. E-mail: cc2762@163.com

© 2017 Chinese Physical Society and IOP Publishing Ltd

transmission electron microscopy (HR-TEM) (Tecnai F30 at an operating voltage of 300 kV). For electrical measurements, both faces of the pellets were coated with silver electrodes approximately 6.5 mm in diameter, and finally heated at 824 °C for 30 min. Dielectric measurements were conducted on the silver electroded, sintered samples using a computer controlled Agilent 4294A LCR meter in a wide frequency (100 Hz–1 MHz) and temperature (300–1023 K) range. The capacitance C, conduction G, and impedance Z data were measured at the sweeping frequency ranging from 100 Hz to 1 MHz and at the temperature ranging from 763 K to 963 K. The electrical data were fitted and simulated by Zview software according to a designed equivalent circuit.

3. Results and discussion

3.1. Crystal structure

X-ray diffraction was performed at room-temperature for the calcinated BIT–NBT powders and Rietveld refinement on the XRD data was conducted using GSAS software with the *I*2*cm* space group of $PbBi_8Ti_7O_{27}$ as CIF starting model.[8] The refinement plots are shown in Fig. 1. Good agreement and low residual are obtained. The XRD diffraction peaks can be well indexed into the *I*2*cm* space group and the refined cell parameters are $a = 5.4716$ Å, $b = 5.4186$ Å, and $c = 73.8526$ Å. Considering the fact that the *I*2*cm* space group possesses a double length of the typical c parameter (~ 37 Å) of BLSFs,[8,9] we tentatively obtained the HR-TEM image of BIT–NBT ceramics along [110] zone axis to further confirm the inter-growth structure, as shown in the inset. The alternating arrangement of four layers of TiO_6 octahedra and three layers of TiO_6 octahedra can be observed in the HR-TEM image. The length for each BIT–NBT unit is calculated to be about 3.7 nm ($\sim c/2$), which further strongly confirms the inter-growth structure of BIT–NBT in our samples.

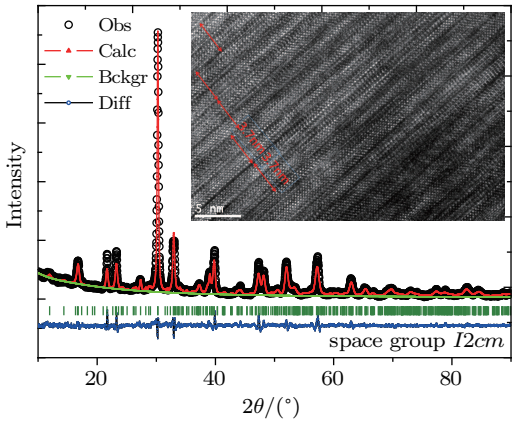


Fig. 1. (color online) XRD refinement plots using GSAS program, the inset shows the HR-TEM image along [110] zone axis for the inter-growth sample.

3.2. Modeling equivalent circuit and relative theory

The ideal impedance behavior can be generally modeled by the Debye expression, where the materials are electrically described as an equivalent circuit composed of a capacitor C and a resistor R in parallel. In most practical cases, however, a non-ideal situation is commonly observed, which is commonly considered as the consequence of diffusive mobility of charge carriers, like mobile ions, hopping electrons, and even dipoles.[10,11]

To model this behavior, a general practice is to place a constant phase element, CPE ($1/[Q(\mathrm{j}w)^m]$), in parallel with a resistor. The CPE element is added to consider the contribution from the oxygen vacancies (OVs)-related defect dipoles to the polarization and conduction process.[10–13] However, only introducing the CPE element still seems to be incomplete as it does not take into account the intrinsic contribution of purely real value C_∞ to the observed capacitance. Generally, C_∞ mainly includes the contributions from the induced atomic, electronic, and ionic lattice polarizations below 1 GHz and a reversible spontaneous polarization above 1 MHz for ferroelectric materials.[14] In our studies on the BIT–NBT system, we concluded that pure C must always be introduced into the equivalent circuit. At present, as shown in Fig. 2, we proposed the equivalent modeling circuit composed of two electrical branches in series representing intragranular properties and the combination effects of grain boundary/electrode-interface, respectively. This modeling leads to the following expression:

$$Z^* = Z_\mathrm{g} + Z_\mathrm{gb}, \tag{1}$$

where

$$Z_\mathrm{gb} = \frac{R_\mathrm{gb}}{1 + C_\mathrm{gb} R_\mathrm{gb} \mathrm{j}\omega}, \tag{2}$$

$$Z_\mathrm{g} = \frac{R_\mathrm{g}}{1 + C_\mathrm{g} R_\mathrm{g} \mathrm{j}\omega + A R_\mathrm{g} (\mathrm{j}\omega)^m}, \tag{3}$$

$\mathrm{j} = \sqrt{-1}$, and ω represents the measuring angular frequency. Parameter A characterizes the contribution of polarizability linked to the universal Jonscher law. Parameter m describes the coupling extent between the charged carriers and the lattice in the polarization process.[15] A lower m generally indicates a stronger ion–ion interaction. Data fitting was performed using the ZView equivalent circuit software. The fitting results demonstrate the predominant response of grains, so our next theoretical analysis will mainly concentrate on the grain branch.

From the equation

$$\begin{aligned} C^*(\omega) &= \frac{1}{\mathrm{j}\omega Z^*} = C_\mathrm{g} + \frac{G_\mathrm{DC}}{\mathrm{j}\omega} + A(\mathrm{j}\omega)^{m-1} \\ &= C' - \mathrm{j}C'', \end{aligned} \tag{4}$$

where $G_{DC} = 1/R_g$, C_g represents the contribution of grain to C_∞, by considering

$$j^{m-1} = \sin\left(\frac{n\pi}{2}\right)^{m-1} - \cos\left(\frac{n\pi}{2}\right)^{m-1},$$

then the real and imaginary parts of the capacitance can be further expressed as

$$C' = C_g + A\sin\left(\frac{n\pi}{2}\right)\omega^{m-1}, \quad (5)$$

$$C'' = \frac{G_{DC}}{\omega} + A\cos\left(\frac{n\pi}{2}\right)\omega^{m-1}. \quad (6)$$

The second terms of Eqs. (5) and (6) characterize the contribution from the OVs-related defect dipoles to the total capacitance. For Eq. (5), at low frequency, the carriers-induced contribution should be dominant whereas C_g could be ignored. For Eq. (6), at low frequency, the G_{DC}/ω term dominates the contribution to the capacitance loss and the contribution from the charge carriers effect is overshadowed.

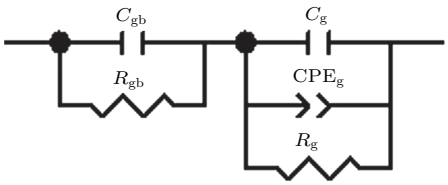


Fig. 2. The proposed modeling equivalent circuit for BIT–NBT sample.

3.3. Electrical properties of BIT–NBT intergrowth-structured sample

Figure 3 presents the temperature dependence curves of C' at selected frequencies. Two capacitance peaks are present at approximately 923 K and 932 K, which correspond to a phase transition within the orthorhombic crystal structure and the Curie transition (T_c), respectively.[16]

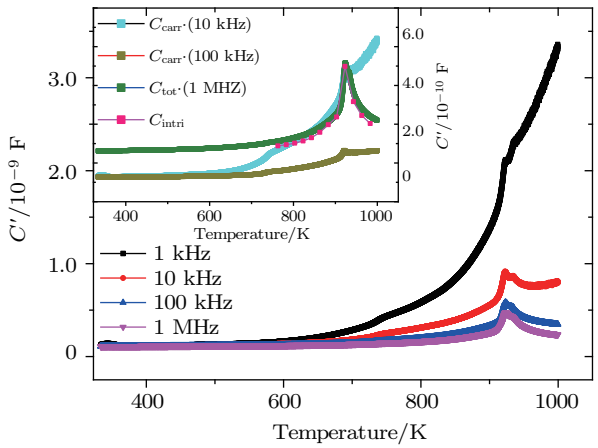


Fig. 3. (color online) The temperature dependence curves of C' at selected frequencies, the inset presents the carrier and intrinsic contributions to the total capacitance.

A frequency-dispersion behavior in capacitance is noticed above 600 K and especially near the T_c region, the capacitance dispersion is strengthened. An uptrend of the capacitance curves appears at high-temperature and low-frequency regions, but disappears at elevated frequencies, which strongly suggests the presence of space-charge effects related to OVs or defects in ferroelectrics.[17] The intrinsic carrier contribution can be calculated from impedance data ($1/C_\infty \approx 1/C_g + 1/C_{gb}$), so it gives a possibility to calculate the individual contributions from intrinsic or OVs-related defect dipoles-induced polarization. As shown in the inset of Fig. 3, the calculated intrinsic capacitance (pink square) nearly equals to the value measured at 1 MHz, indicating that above 1 MHz, the OVs-related defect dipoles can no longer respond to the ac external field and the carrier-induced capacitance is almost null. The OVs-related defect dipoles mobilize easier and consequently dominate the capacitance response.

The frequency dependences of capacitances C' and C'' at selected temperatures are presented in Figs. 4(a) and 4(b), respectively. The red line represents the simulation line according to the equivalent circuits in Fig. 2. Good fitting is obtained except for the interference effects from the measurement machine. Two distinguishable regions are present: a strong low-frequency dispersion region and a high-frequency plateau region, which correspond to the dominant contribution from the OVs-related defect dipoles and the intrinsic response, respectively. The plateau also well confirms the rationality of CQR circuit elements. It is noticed that the carrier-induced contribution is much strengthened with elevated temperatures especially around T_c. However, in the inset of Fig. 4(a), an opposite change above T_c is present in the intrinsic capacitance, exhibiting the decreasing trend, which can be linked to the sharp reduction in capacitance from grains and grain boundaries due to the Curie phase transition there. From the C'' curves in Fig. 4(b), perfect linear lines in the double-logarithmic plots are observed above T_c, indicating that the capacitance behavior is dominated by dc conductivity G_{DC}/ω term in Eq. (6). This behavior can be characterized by the universal power law[18]

$$C'' = B\omega^s, \quad (7)$$

where B and s ($-1 < s < 0$) are temperature-dependent parameters. Generally, exponent s actually scales the extent of localization for the OVs-related defect dipoles,[18,19] e.g., in the case of $s = -1$, equation (7) presents the usual reciprocal frequency behavior, which corresponds to the non-dispersive transport process for free charge carriers; for $s = 0$, equation (7) can be deduced to $C'' =$ constant,[20] which is characteristic of almost constant values associated with strictly localized charge carriers. As for $-1 < s < 0$, the system follows the universal power law with confined hopping carriers. Obviously the s exponent for our sample linearly decreases with

elevated temperatures until T_c (923 K), and it nearly reaches a saturation value of -1. Therefore, it can be rationally concluded that below T_c, the charge carriers are localized and only make short-range hopping movement, but above T_c, the carriers are delocalized and become free ones, thus contributing to the long-range dc conduction process.

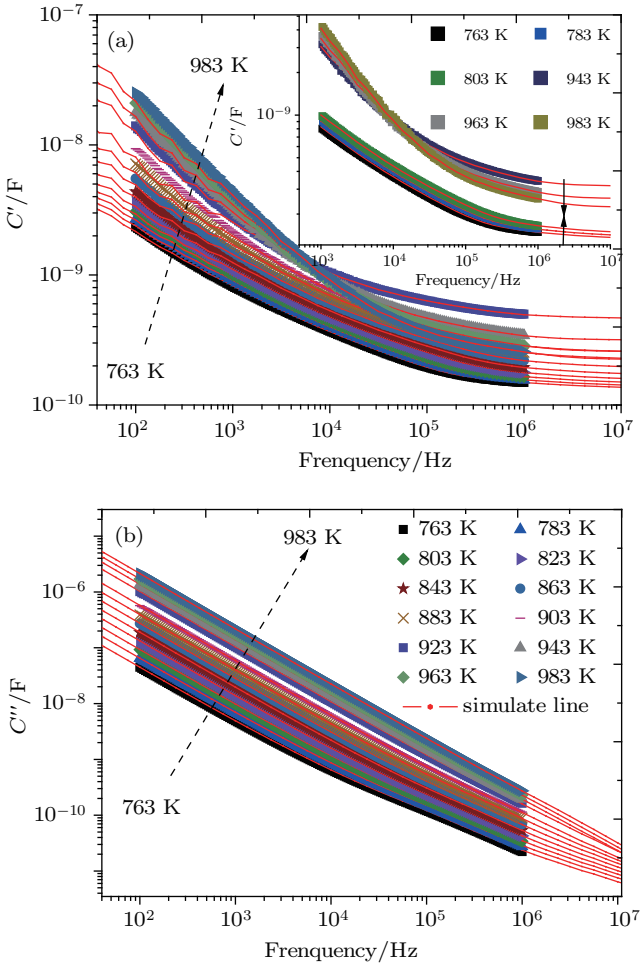


Fig. 4. (color online) The frequency dependences of (a) C' and (b) C'' at selected temperatures.

Another widely accepted method to probe into electrical behaviors is plotting the complex impedance curves. Figure 5 presents the Z'' vs. Z' plots (Nyquist plots) at selected temperatures. A simulation of complex impedance was conducted with the designed (CQR) equivalent circuit and an excellent fitting to the experimental data was obtained. The fitting results further confirm that at the entire measuring temperature range only grain is significant. Careful observation of Fig. 5 reveals that at the high frequencies region a typical Debye-type behavior appears with a tangent angle close to 90° at $f \to \infty$ between the plot and the real Z' axis, whereas at the low frequencies side the observed behavior is similar to the typical Cole–Cole type with a tangent angle lower than 90° at $f \to 0$ Hz. These observations are attributed to the predominance of the intrinsic response at high frequency and the charge carriers-induced response at low frequency side, respectively.[14] Taking grains as a representative, from Eq. (3), at the high-frequency region, the term $AR_g(j\omega)^m$ is almost null, thus giving Debye-type behavior. However, at the low-frequency region, the term $C_gR_gj\omega$ can be ignored, thus giving the typical Cole–Cole type.

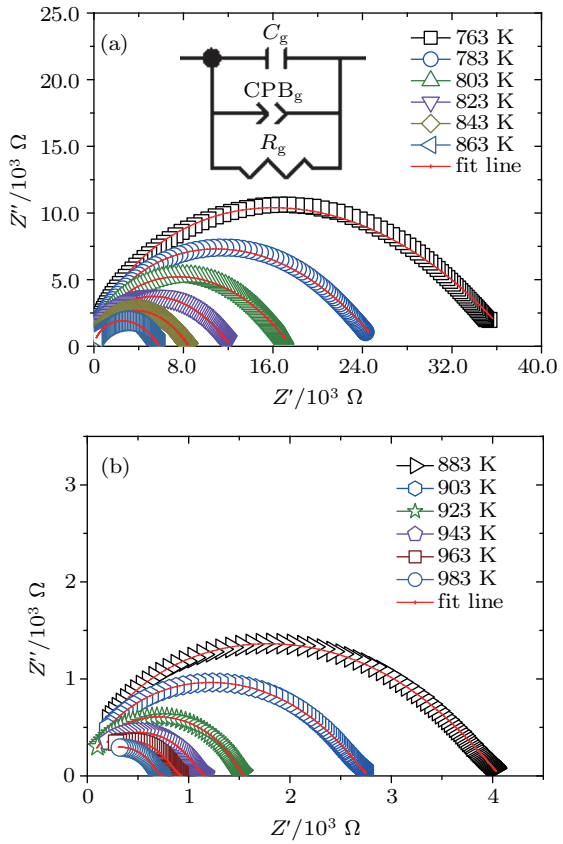


Fig. 5. (color online) Complex impedance plots corresponding to (a) 763–863 K and (b) 883–983 K.

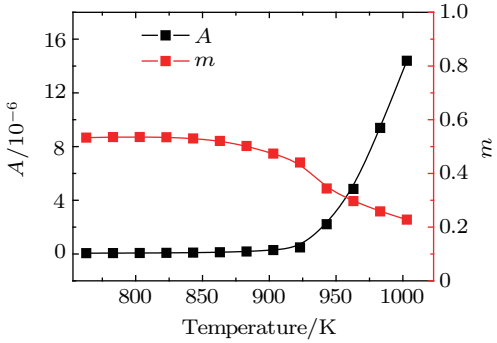


Fig. 6. (color online) The behaviors of parameters A and m with the elevated temperatures.

Figure 6 shows parameters A and m plotted as a function of temperature. Both parameters A and m exhibit an almost constant behavior with the elevated temperature below 923 K (T_c). However, the trends fail to persist above T_c where m begins to decrease, whereas A reveals an obvious increase. The deviation around T_c rationally concludes that the contribution from the charged carriers in the polarization process is

strengthened above T_c, which further emphasizes the conclusions in Figs. 3 and 4. The impedance data can be further plotted in forms of electrical modulus expressed as $M^* = j\omega C_0 Z^*$.

To further confirm the behaviors of the charge carriers, we compare the plots between the normalized impedance (Z'') and modulus (M'') in Fig. 7. A distinguishable mismatch between Z'' and M'' peaks is present below 923 K. This confirms that the carriers are localized ones and have no contribution to long-range conduction.[19,21] The mismatch becomes smaller with elevated temperature until the two peaks nearly overlap at a particular frequency above 923 K, which suggests that the carriers are delocalized and contribute to long-range conduction.[22] These results indicate that the relaxing species for the relaxations below T_c and above T_c in our sample are correlated with the localized carriers and the delocalized species, respectively.

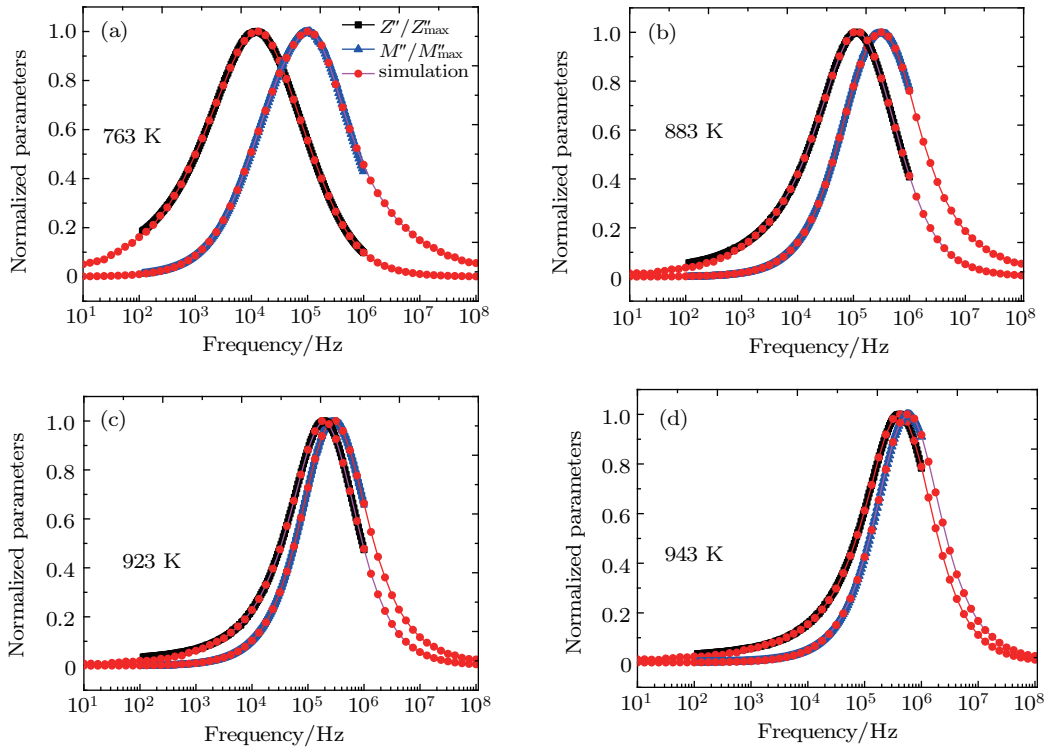


Fig. 7. (color online) The comparison plots between impedance Z'' and modulus M'' at (a) 763 K, (b) 883 K, (c) 923 K, and (d) 943 K.

In order to further confirm the deviation of the relaxing species below T_c and above T_c, figure 8 presents the plots of relaxing frequency $\ln(f_{M''\max})/\ln(f_{Z''\max})$ vs. $1000/T$ for grains. Obviously, the Arrhenius plots of $\ln(f_{M''\max})$ vs. $1000/T$ and $\ln(f_{Z''\max})$ vs. $1000/T$ can be fitted into two linear lines and a deviation point from the Arrhenius relation occurs at 923 K. Below 923 K, the activation energies are calculated to be ~ 0.79 eV and ~ 1.05 eV for $\ln(f_{M''\max})$ and $\ln(f_{Z''\max})$, respectively; and above 923 K, almost the same activation energies are obtained and found to be ~ 1.6 eV. This fact implies that different mechanisms dominate the relaxation processes at the two temperature ranges. The high-temperature relaxation or conduction process in ferroelectric ceramics is generally linked to the short-range migration or long-range hopping movement of charged OVs, respectively.[23,24] Double-ionization of OVs occurs at and above 800 K and about 1 eV activation energy is required for the short-range hopping movement of the doubly positively charged state. This result is in good agreement with our experimental results below T_c in Fig. 7. Based on the results above, it can be rationally suggested that at this temperature range of 763–923 K, the relaxation mechanism should be linked to the movement of OVs. The short-range hopping of doubly-ionized OVs, equivalent to the reorientation of the dipoles, induces the relaxation process.[25]

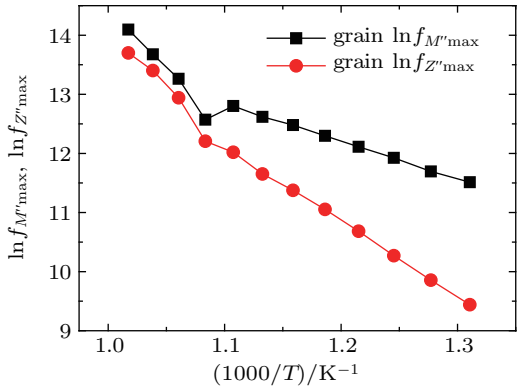


Fig. 8. (color online) The Arrhenius plots of $\ln(f_{M''\max})$ vs. $1000/T$ and $\ln(f_{Z''\max})$ vs. $1000/T$.

Above T_c, the doubly-ionized OVs-related carriers are delocalized and become free ones. These free carriers make long-range movements and contribute to the long-range conduction, which will cause the reduction in relaxation species and thus give rise to a greater relaxation activation energy of ~ 1.6 eV. These results are also consistent with the observations in the inset of Fig. 3, where around T_c charge carrier contributions also induce a capacitance peak. This is because above T_c, the carriers are greatly delocalized and contribute to the significant increase in C'' through Eq. (6), but have no contribution to C'. Therefore, when the doubly charged OVs become free carriers, a C' peak will inevitably appear. These observations account well for our assumptions on the relaxation mechanisms. For BLSFs, the conductivity behavior is mainly derived from the perovskite layers and the $(Bi_2O_2)^{2+}$ layers are rigid insulative.[26]

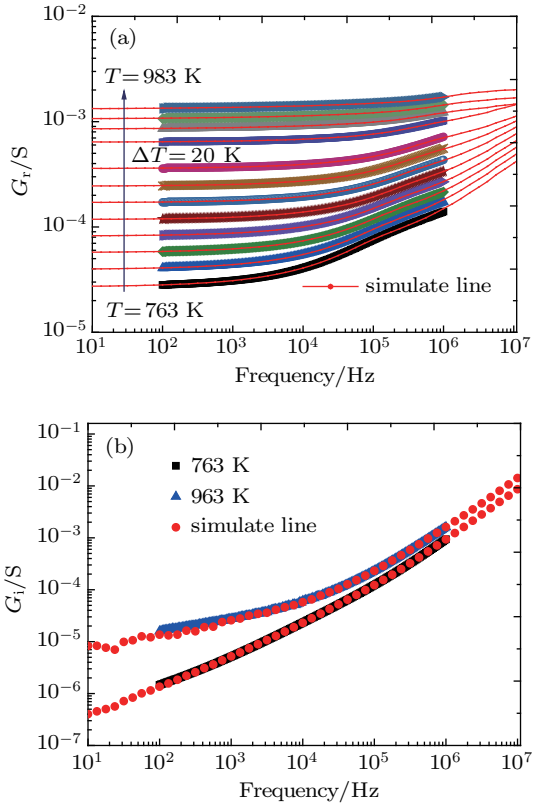


Fig. 9. (color online) Behaviors of the real G_r (a) and imaginary G_i (b) parts of conduction at different temperatures and frequencies.

To further check our assumptions, we therefore perform analysis on the conduction behaviors as shown in Fig. 9. In Fig. 9(a), the low-frequency plateau region characterizes the dc conductivity. We note that with elevated temperature, the dc conductivity contribution is strengthened and nearly dominates the total conductivity above 923 K. Figure 9(b) presents the behavior of the imaginary part of conduction with elevated temperature, where the slope at low frequency between G_i and ω is obviously weakened above T_c. In Eq. (5), it can be deduced that at low frequency the second term $C' = A\sin(n\pi/2)\omega^{m-1}$ is dominant. The weakened slope also implies the certainty of the decreased m (in Fig. 6). Therefore, based on the analysis above, we suggest that these observations can be ascribed to the delocalization of carriers above T_c, which dominates the contributions to the long-range dc conductivity.

Next, we extract the fitted dc conductivity and plot them against $1000/T$ in Fig. 10(a), where a deviation occurs around T_c, and the activation energies from the Arrhenius relation are calculated to be ~ 0.93 eV and ~ 1.09 eV below and above T_c, respectively. Similar results are found in the ac conductivity in Fig. 10(b) conducted at 1 kHz. As mentioned above, with the elevated temperature up to T_c, the localized charged OVs are delocalized and become free ones, which makes contributions to the dc conductivity. The increase in activated conduction species will contribute to the lower activation energies.

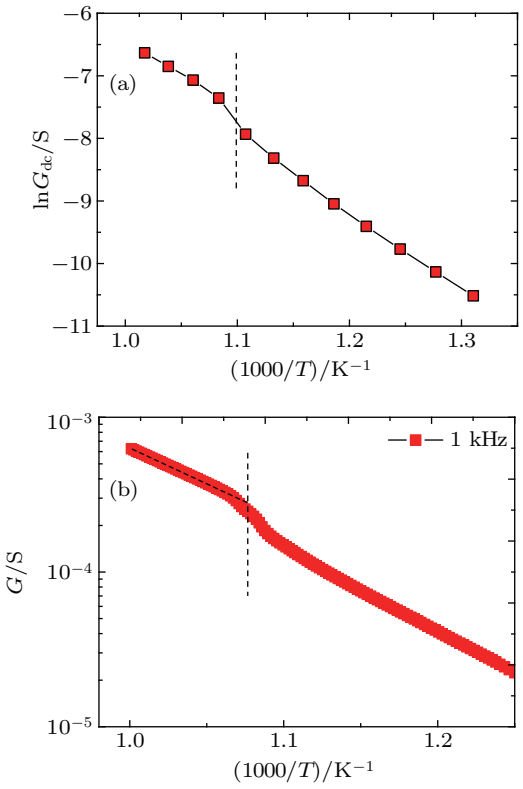


Fig. 10. (color online) The fitted dc conductivity (a) and ac conductivity (b) at 1 kHz.

4. Conclusion

Inter-growth bismuth layer-structured BIT–NBT ceramics were successfully synthesized via the traditional solid-state reaction method. Rietveld refinement on XRD data was conducted. Good agreements and low residuals are obtained. The XRD peaks can be well indexed into $I2cm$ space group and the refined lattice parameters are $a = 5.4716$ Å, $b = 5.4186$ Å, and $c = 73.8526$ Å. Dielectric and impedance properties were systematically analyzed. A strong dielectric dispersion at low-frequency region was observed, which was associated with the

presence of ionized OVs-related defect dipoles related to oxygen vacancies or defects. Relaxation and conduction mechanisms were determined on the basis of the electrical behaviors and a proper equivalent circuit. Grain response dominates the impedance plots. At the temperature range 763–923 K below T_c, doubly ionized OVs are localized and the short-range hopping leads to the relaxation process with an activation energy 0.79–1.01 eV. Above T_c, the doubly charged OVs are delocalized and become free ones, contributing to the long-range dc conduction. The reduction in relaxation species gives rise to a higher relaxation activation energy ~ 1.6 eV.

References

[1] Kikuchi T 1976 *J. Less-common Metals* **48** 319
[2] Kikuchi T, Watanabe A and Uchida K 1977 *Mater. Res. Bull.* **12** 299
[3] Yi Z G, Li Y X, Wen Z Y and Wang S R 2005 *Appl. Phys. Lett.* **86** 192906
[4] Noguchi Y, Miyayama M and T Kudo 2000 *Appl. Phys. Lett.* **77** 3639
[5] Wang H, Li J, Xu J W, Yang L and Zhou S J 2011 *Adv. Mater. Res.* **197** 1781
[6] Maalal R, Manier M and Mercurio J P 1995 *J. Eur. Ceram. Soc.* **15** 1135
[7] Tuohig W D and Tien T Y 1980 *J. Am. Ceram. Soc.* **63** 595
[8] Tellier J, Boullay P and Mercurio D 2007 *Z. Kristallogr.* **222** 234
[9] Parida G and Bera J 2014 *Phase Transitions.* **87** 452
[10] Jonscher A K 1976 *Thin Solid Films.* **36** 1
[11] Jonscher A K 1977 *Nature.* **267** 673
[12] Yuan C L, Liu X Y, Zhou C R, Xu J W and Yang Y 2011 *Chin. Phys. B* **20** 048701
[13] Asma B A and Muhammad J A 2011 *Chin. Phys. B* **20** 058102
[14] Lu Z, Bonnet J P, J Ravez and Hagenmuller P 1992 *Solid State Ionics* **57** 235
[15] Kajewski D and Ujma Z 2013 *Ceram. Int.* **39** 8213
[16] Yokoi A and Sugishita J 2008 *J. Alloys Compd.* **452** 467
[17] Zhang T F, Tang X G and Liu Q X 2015 *J. Am. Ceram. Soc.* **98** 551
[18] Jonscher A K 1999 *J. Phys. D: Appl. Phys.* **32** R57
[19] Wang C C, Lei C M and Wang G J 2013 *J. Appl. Phys.* **113** 094103
[20] Nowick A S and Lim B S 2001 *Phys. Rev. B* **63** 184115
[21] Li W and Schwartz R W 2007 *Phys. Rev. B* **22** 012104
[22] Nobre M A L and Lanfredi S 2000 *Chromatographia* **51** S98
[23] Panlener R J and Blumenthal R N 2006 *J. Am. Ceram. Soc.* **54** 610
[24] Waser R, Tudor B and Härdtl K H 1990 *J. Am. Ceram. Soc.* **73** 1645
[25] Chen A, Yu Z and Cross L E 2000 *Phys. Rev. B.* **62** 228
[26] Changbai Long, Huiqing Fan and Pengrong Ren 2013 *Inor. Chem.* **52** 5045